Available online at www.sciencedirect.com
SCIENCE DIRECT®
Acta Materialia 53 (2005) 1179–1190
Acta MATERIALIA
www.actamat-journals.com

Representation of misorientations in Rodrigues–Frank space: application to the Bain, Kurdjumov–Sachs, Nishiyama–Wassermann and Pitsch orientation relationships in the Gibeon meteorite

Youliang He *, Stéphane Godet, John J. Jonas

Department of Metals and Materials Engineering, McGill University, Wong Building, 3610 University Street, Montreal, Que., Canada H3A 2B2

Received 7 July 2004; received in revised form 14 September 2004; accepted 5 November 2004
Available online 24 December 2004

Abstract

The three classical orientation relationships describing the γ-to-α transformation, namely the Bain, Kurdjumov–Sachs (K–S) and Nishiyama–Wassermann (N–W), are represented in Rodrigues–Frank (R–F) space. Two alternative reference systems are used to highlight the differences between the three types of misorientation. Some observations obtained on the Gibeon meteorite are analyzed using the two classes of reference system to reveal features of the transformation under conditions of very slow cooling. It is shown that the Bain correspondence relations are never satisfied, while the measurements fall in the full range of direction parallel conditions extending from the K–S to the N–W. The crystallographic features of the Pitsch orientation relation are presented in R–F space in Appendix A. The experimental observations conform to this type of transformation to a considerably lesser extent than to the classical K–S and N–W relations.

Keywords: Metals; Phase transformation; Misorientation; EBSD; Rodrigues–Frank space

1. Introduction

Misorientation, the crystallographic orientation difference between two individual crystallites, is an important parameter used to describe the microtexture of materials. For instance, the grain boundary texture is commonly specified in terms of a rotation about an axis common to both crystallites that brings the coordinate system of the first into coincidence with that of the other. This is the so-called angle–axis pair description and it provides significant information about the grain boundary geometry. An important example is that of coincident site lattice (CSL) boundaries, which are uniquely described by the axis and angle of misorientation between the two neighboring grains [1].

In other cases, such as phase transformations, where the misorientation between the initial phase and its transformed products is the major concern, it is more convenient to represent the misorientation between the two phases using the Rodrigues–Frank (R–F) vector, since the latter takes the lowest angle solution and integrates the four parameters (i.e. the rotation angle and the three components of the rotation axis) into a three-component vector that can be readily displayed in a three-dimensional Cartesian space (R–F space) [2]. One of the advantages of R–F parameterization is that either the specimen or the crystal axes can be chosen for reference; according to this system of representation, the rotation angle and axis are directly related to a

* Corresponding author. Tel.: +1 514 3984755x09501; fax: +1 514 3984492.
E-mail address: youliang.he@mail.mcgill.ca (Y. He).

1359-6454/$30.00
doi:10.1016/j.actamat.2004.11.021

vector drawn from the center of the space to the point representing the rotation axis.

The use of R–F space to represent orientations and misorientations is relatively new compared to that of using rotations about three successive axes, i.e. that of Euler space, and its advantages over the employment of such other spaces have been addressed by several researchers [3–5]. However, most of these investigations were focused on the representation of *orientations* in R–F space; only a few were concentrated on the representation of *misorientations* [2,6,7]. In this study, the misorientation between two crystallites, which is calculated from orientations measured by electron backscatter diffraction (EBSD) techniques, is represented as an R–F vector, taking one of the crystallites as the reference system. Specifically, the three classical correspondence relationships that describe the FCC to BCC transformation, namely the Bain [8], Kurdjumov–Sachs [9] and Nishiyama–Wassermann [10,11], are represented in this space. A second reference system is then introduced, which has certain advantages in the present case.

The variants of the three orientation relationships are derived directly from the parallelism conditions applying to the crystallographic planes and directions that define these relationships. Some recent results concerning the transformation of taenite (FCC austenite) in the Gibeon meteorite are then presented to illustrate the advantages of the use of this space. In Appendix A, the variants of the Pitsch [12] transformation relationship are also derived from the parallelism conditions. These are then represented in R–F space using the two frames of reference (austenite and Bain). Their positions on a {0 0 1} pole figure are compared with those of K–S and N–W. Some meteorite observations are then plotted in these two forms of representation (pole figure and R–F space) and the extent to which the Pitsch relation applies is evaluated.

2. Misorientation and Rodrigues–Frank space

Here, the orientation matrices for two crystallites **A** and **B** are $\mathbf{M}_A$ and $\mathbf{M}_B$, respectively. Then the *misorientation* matrix $\mathbf{M}_{AB}$ relating these crystallites, arbitrarily taking crystallite **A** as the reference system, can be written as

$$\mathbf{M}_{AB} = \mathbf{M}_B \mathbf{M}_A^{-1}. \quad (1)$$

This matrix defines a rotation that transforms the coordinate system of the reference crystallite into coincidence with that of the other crystallite. [1] The angle–axis form associated with this misorientation matrix can then be calculated as: $\theta = \arccos(\frac{1}{2}[\mathrm{Tr}(\mathbf{M}_{AB}) - 1])$ and $[u, v, w] = [m_{23} - m_{32}, m_{31} - m_{13}, m_{12} - m_{21}]$ [13], where $\mathrm{Tr}(\mathbf{M}_{AB})$ is the trace of matrix $\mathbf{M}_{AB}$ and m_{ij} $(i, j = 1, 2, 3)$ are the elements of $\mathbf{M}_{AB}$.

The four parameters can be further reduced to three using the Rodrigues formula: $\mathbf{R} = \tan\frac{\theta}{2}[u, v, w]$ [14], which defines the three components $(\mathbf{R}_1, \mathbf{R}_2, \mathbf{R}_3)$ of the R–F vector. Each misorientation is now represented as an R–F vector or more specifically as the endpoint of the vector in R–F space. To avoid the singularity associated with the R–F vector approaching infinity when the rotation angle θ reaches its upper limit π, the space is reduced to a finite subspace called the *fundamental zone* by utilizing the minimum angle–axis pair representation or *disorientation*. The latter is obtained by taking the crystal symmetry into account, i.e. employing the 24 symmetry operations for cubic crystals [4,7].

The fundamental zone of R–F space for cubic symmetry is reproduced here in Fig. 1 since most of the discussion that follows about the four transformation relationships will be presented in this subspace. Some authors have reduced the fundamental zone even further by considering only 1/48 of this space [7]. However, this approach is not satisfactory for the present study since, as will be evident in what follows, both the signs and orders of the components of the rotation axis are of importance.

The three points A, B and C illustrated in the diagram typify the centers of the octahedral (A) and triangular (B) faces of the fundamental zone, while the vertices of the triangles are characterized by C. There are 6, 8 and 24, respectively, such points in the fundamental zone. It should be emphasized that it is a prop-

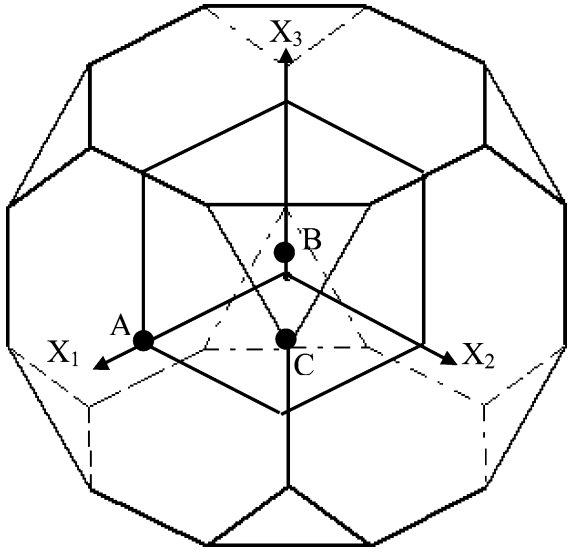

Fig. 1. Fundamental zone of R–F space for cubic symmetry. The three illustrated points correspond to the following angle–axis pairs: A: 45° [1 0 0], B: 60° [1 1 1] and C: 62.8° $[1\,1\,(\sqrt{2}-1)]$.

[1] It should be noted that the matrices used here are associated with the coordinate frame transformations that are often cited in material science rather than the body rotations usually employed in other fields. Moreover, the transformation is always expressed as a conversion of the reference coordinate system into that of the product.

erty of R–F space that points on the boundary faces have their equivalents on the opposite faces [7]. For instance, points on the octahedra (the {1 0 0} bounds) have their equivalents on the opposite faces but these are offset by rotations through π/4 about the corresponding ⟨1 0 0⟩ axis. Similarly, points on the triangles (the {1 1 1} bounds) have their equivalents on the opposite faces but offset by rotations through π/3 about the ⟨1 1 1⟩ axis [15].

3. Bain, K–S and N–W relationships in R–F space

The parallelism conditions for the four orientation relationships considered here, namely the Bain, K–S, N–W and Pitsch, are summarized in Table 1 [16]. Also included are the minimum angle–axis pairs and the corresponding R–F vectors derived from the parallelism relationships. The pole figure representation of the three classical γ-to-α transformation relationships is shown in Fig. 2, where the {1 0 0} poles of the product phase are projected onto the parent (1 1 1) plane. The K–S variants are numbered in terms of the associated γ slip systems denoted using the nomenclature of Bishop and Hill [17,18]. The Pitsch representation is provided in Appendix A.

It is clear from Fig. 2 that the K–S and N–W variants are clustered around the Bain variants and that there are eight of the K–S and four of the N–W variants around each Bain. Each N–W variant is located between a pair of K–S variants, e.g. N–W variant 1 is located between K–S variants 7 and 20. These three form a set of *coplanar* variants that are characterized by having their crystallographic $\{1\,1\,0\}_\alpha$ planes parallel to the same $\{1\,1\,1\}_\gamma$ plane. This can be seen from Table 2, where the variants of the Bain, K–S and N–W relationships are listed together with the detailed parallelism conditions that apply to the crystallographic planes and directions of the two phases.

It is important to note that the direction parallelism specified by the K–S relationship, which is that of close-packed directions in the two phases, calls for the pair of coplanar K–S variants to have their crystallographic $\langle 1\,1\,0\rangle_\gamma$ directions parallel to the same $\langle 1\,1\,1\rangle_\alpha$ direction. These are 10.53° away from each other in R–F space. Each K–S variant also has a closely spaced *non-coplanar* variant, which is again 10.53° away in R–F space. For example, K–S variants 1(aI) and 7(cI) are closely spaced non-coplanar variants. These two products are *cross-slip related* in terms of the slip systems, which means that the two variants are associated with dislocations on intersecting slip planes [19].

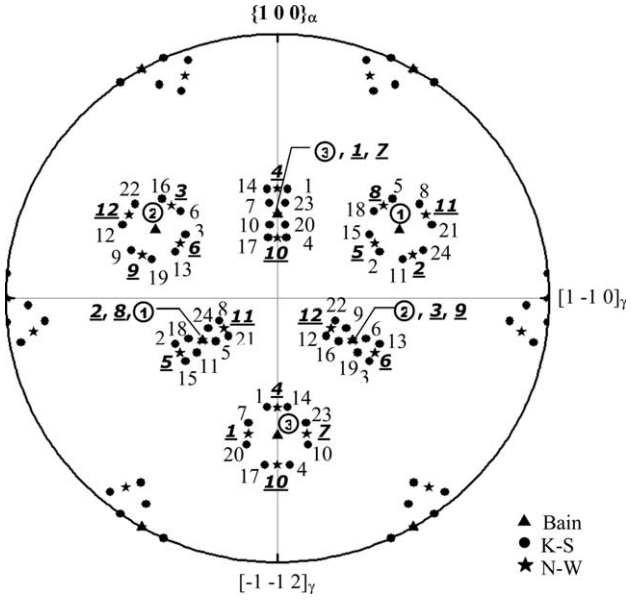

Fig. 2. Stereographic plot of $\{1\,0\,0\}_\alpha$ poles for the Bain, K–S and N–W variants projected onto the $(1\,1\,1)_\gamma$ plane. Circled and underlined numbers represent the Bain and N–W variants, respectively.

If the coordinate system of the parent crystal is taken as the reference system, which corresponds to matrix $\mathbf{M}_A$ in Eq. (1), the variants of the three correspondence relationships can be illustrated in R–F space as shown in Fig. 3. From this figure and Table 1, it can be seen that the numbers of minimum angle–axis variants, and thus the numbers of R–F vectors, for the Bain, N–W and K–S relationships are 6, 24 and 24, respectively. These

Table 1
Orientation relationships between γ and α

Orientation relationship	Parallelism	Number of variants	Minimum angle–axis pairs	R–F vectors
Bain	$\{0\,0\,1\}_\gamma//\{0\,0\,1\}_\alpha$ $\langle 1\,0\,0\rangle_\gamma//\langle 1\,1\,0\rangle_\alpha$	3	45° ⟨1 0 0⟩	⟨0.414 0 0⟩ (6 points)
Kurdjumov–Sachs (K–S)	$\{1\,1\,1\}_\gamma//\{1\,1\,0\}_\alpha$ $\langle 1\,1\,0\rangle_\gamma//\langle 1\,1\,1\rangle_\alpha$	24	42.85° ⟨0.968 0.178 0.178⟩	⟨0.380 0.07 0.07⟩ (24 points)
Nishiyama–Wassermann (N–W)	$\{1\,1\,1\}_\gamma//\{1\,1\,0\}_\alpha$ $\langle 1\,1\,2\rangle_\gamma//\langle 1\,1\,0\rangle_\alpha$	12	45.98° ⟨0.976 0.083 0.201⟩	⟨0.414 0.035 0.085⟩ (24 points)
Pitsch (P)	$\{1\,0\,0\}_\gamma//\{1\,1\,0\}_\alpha$ $\langle 0\,1\,1\rangle_\gamma//\langle 1\,1\,1\rangle_\alpha$	12	45.98° ⟨0.083 0.201 0.976⟩	⟨0.035 0.085 0.414⟩ (24 points)

Table 2
The Bain, K–S and N–W variants

Bain variant	Coplanar N–W and K–S variants		$\{111\}_\gamma//\{110\}_\alpha$		$\langle 110\rangle_\gamma$ or $\langle 112\rangle_\gamma//\langle 111\rangle_\alpha$ or $\langle 110\rangle_\alpha$	
1	***N–W***	***5***	a (1 1 1)	***(0 1 1)***	***[2 −1 −1]***	***[0 −1 1]***
	K–S	2 (aII)		(−1 0 1)	[−1 0 1]	[−1 −1 −1]
		15 (−aIII)		(−1 1 0)	[−1 1 0]	
	N–W	***8***	b (−1 −1 1)	***(0 −1 1)***	***[−2 1 −1]***	***[0 1 1]***
$(100)_\gamma//(100)_\alpha$	K–S	5 (bII)		(1 0 1)	[1 0 1]	[1 1 −1]
		18 (−bIII)		(1 −1 0)	[1 −1 0]	
	N–W	***11***	c (−1 1 1)	***(0 1 1)***	***[2 1 1]***	***[0 1 −1]***
$[010]_\gamma//[011]_\alpha$	K–S	8 (cII)		(1 0 1)	[1 0 1]	[1 −1 −1]
		21 (−cIII)		(1 1 0)	[1 1 0]	
	N–W	***2***	d (1 −1 1)	***(0 −1 1)***	***[−2 −1 1]***	***[0 −1 −1]***
	K–S	11 (dII)		(−1 0 1)	[−1 0 1]	[−1 1 −1]
		24 (−dIII)		(−1 −1 0)	[−1 −1 0]	
2	***N–W***	***6***	a (1 1 1)	***(1 0 1)***	***[−1 2 −1]***	***[1 0 −1]***
	K–S	3 (aIII)		(1 −1 0)	[1 −1 0]	[−1 −1 −1]
		13 (−aI)		(0 −1 1)	[0 −1 1]	
	N–W	***3***	b (−1 −1 1)	***(−1 0 1)***	***[1 −2 −1]***	***[−1 0 −1]***
$(010)_\gamma//(010)_\alpha$	K–S	6 (bIII)		(−1 1 0)	[−1 1 0]	[1 1 −1]
		16 (−bI)		(0 1 1)	[0 1 1]	
	N–W	***9***	c (−1 1 1)	***(−1 0 1)***	***[−1 −2 1]***	***[1 0 1]***
$[001]_\gamma//[101]_\alpha$	K–S	9 (cIII)		(−1 −1 0)	[−1 −1 0]	[1 −1 −1]
		19 (−cI)		(0 −1 1)	[0 −1 1]	
	N–W	***12***	d (1 −1 1)	***(1 0 1)***	***[1 2 1]***	***[−1 0 1]***
	K–S	12 (dIII)		(1 1 0)	[1 1 0]	[−1 1 −1]
		22 (−dI)		(0 1 1)	[0 1 1]	
3	***N–W***	***4***	a (1 1 1)	***(1 1 0)***	***[−1 −1 2]***	***[−1 1 0]***
	K–S	1 (aI)		(0 1 −1)	[0 1 −1]	[−1 −1 −1]
		14 (−aII)		(1 0 −1)	[1 0 −1]	
	N–W	***10***	b (−1 −1 1)	***(−1 −1 0)***	***[1 1 2]***	***[1 −1 0]***
$(001)_\gamma//(001)_\alpha$	K–S	4 (bI)		(0 −1 −1)	[0 −1 −1]	[1 1 −1]
		17 (−bII)		(−1 0 −1)	[−1 0 −1]	
	N–W	***1***	c (−1 1 1)	***(−1 1 0)***	***[−1 1 −2]***	***[−1 −1 0]***
$[100]_\gamma//[110]_\alpha$	K–S	7 (cI)		(0 1 −1)	[0 1 −1]	[1 −1 −1]
		20 (−cII)		(−1 0 −1)	[−1 0 −1]	
	N–W	***7***	d (1 −1 1)	***(1 −1 0)***	***[1 −1 −2]***	***[1 1 0]***
	K–S	10 (dI)		(0 −1 −1)	[0 −1 −1]	[−1 1 −1]
		23 (−dII)		(1 0 −1)	[1 0 −1]	

The γ {1 1 1} planes and K–S variants are identified using the notation of Bishop and Hill.

should be compared with the numbers of variants that are evident on the pole figure (3, 12 and 24, respectively). Note that there are twice as many variants for the Bain and N–W relationships in R–F space as in the pole figure because the endpoints of these variants in R–F space are located on the external surfaces of the fundamental zone; as a result, each point has its equivalent on the opposite surface. By contrast, the endpoints of the K–S variants are situated on the six planes located at a normalized distance of 0.918 from the origin, with four points on each plane (i.e. these planes are *inside* the fundamental zone).

As indicated above, the endpoints of the Bain and N–W variants reside *on* the six octahedra of the fundamental zone. Here, one Bain variant is located at the center of each face and four N–W variants reside around it. These relationships are clarified in Fig. 3(b) and (d), where all the points contained in the R–F space of Fig. 3(b) are projected onto the bottom face in Fig. 3(d). The two Bain variants on the top and bottom faces are collapsed into one point in the center.

In a similar manner, the eight K–S variants on opposite planes in Fig. 3(a) are represented by four overlapping points in Fig. 3(c) [1(14), 23(10), 20(7) and 4(17)]. Note that, in contrast to the K–S case of Fig. 3(c), the four N–W points on each of the opposite faces of Fig. 3(b) are not superimposed. As a result, eight N–W vectors and four K–S vectors can be seen around each Bain axis in the two projected views, which is just the opposite of the pole figure view, where four N–W variants and eight K–S variants can be seen around each Bain variant. The "supplementary" N–W variants are numbered $13, 14, \ldots, 24$ here; these correspond to the "original" set of $1, 2, \ldots, 12$, respectively. The reason for this

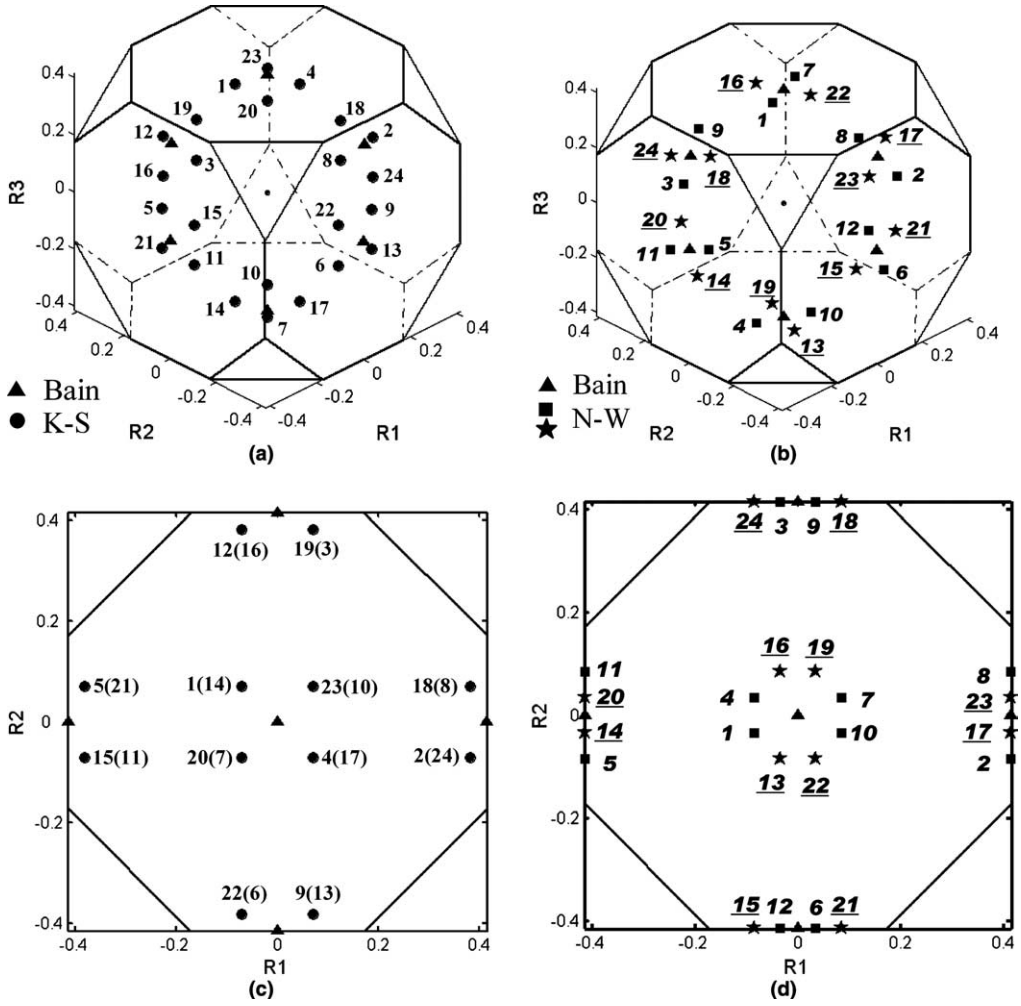

Fig. 3. The Bain, K–S and N–W orientation relationships represented in the fundamental zone of R–F space: (a) the Bain and K–S relationships, (b) the Bain and N–W relationships, (c) projection of (a) onto the bottom face, (d) projection of (b) onto the bottom face. The K–S variants are numbered according to their associated Bishop–Hill slip systems, numbers in brackets being variants on the bottom plane. Underlined numbers represent the equivalent N–W variants induced by symmetry rotations.

apparent redundancy will be taken up below after a second frame of reference is introduced.

This situation is changed if one chooses one of the Bain variants, rather than the parent γ grain, as the reference system. As illustrated in Fig. 4, in this case 24 K–S and 12 N–W variants can be seen, just as in the pole figure representation. The relation between the K–S and N–W variants around the reference Bain variant (in the centers of Fig. 4(c) and (d)) also resembles that of the pole figure, with one N–W variant between pairs of K–S variants. Under such conditions, the other two Bain variants are located at the vertices of the fundamental zone, which are the triple junctions of three boundary faces (two $\{100\}$ bounds and one $\{111\}$ bound). As noted above, each point on a boundary face has an equivalent on the opposite face. Consequently, there are four equivalent points for each of the two remaining Bain variants, one on each of the four pairs of opposing bounds. Therefore, in Fig. 4, there are a total of eight Bain points on the triangular faces in addition to the one located at the center of the figure (the reference Bain variant).

The geometry of R–F space as employed here can be summarized as follows. A point situated *inside* the fundamental zone is *unique*. This is the case for the 24 K–S variants or the 12 N–W variants when a Bain variant is taken as the frame of reference. A point that is situated on a *face* of the fundamental zone has *one equivalent* on the opposite face, for a total of two points (multiplicity of 2). These points are rotated by 45° $\langle 100 \rangle$ about the center of the opposite face if they lie on an octahedron, or by 60° $\langle 111 \rangle$ if they lie on a triangle.

This is the case for the R–F vectors that correspond to the Bain and N–W relationships when the austenite is chosen as the reference frame. Similarly, a point that lies on an *edge* of the fundamental zone is shared by two faces and, therefore, has *one equivalent point* on *each* of

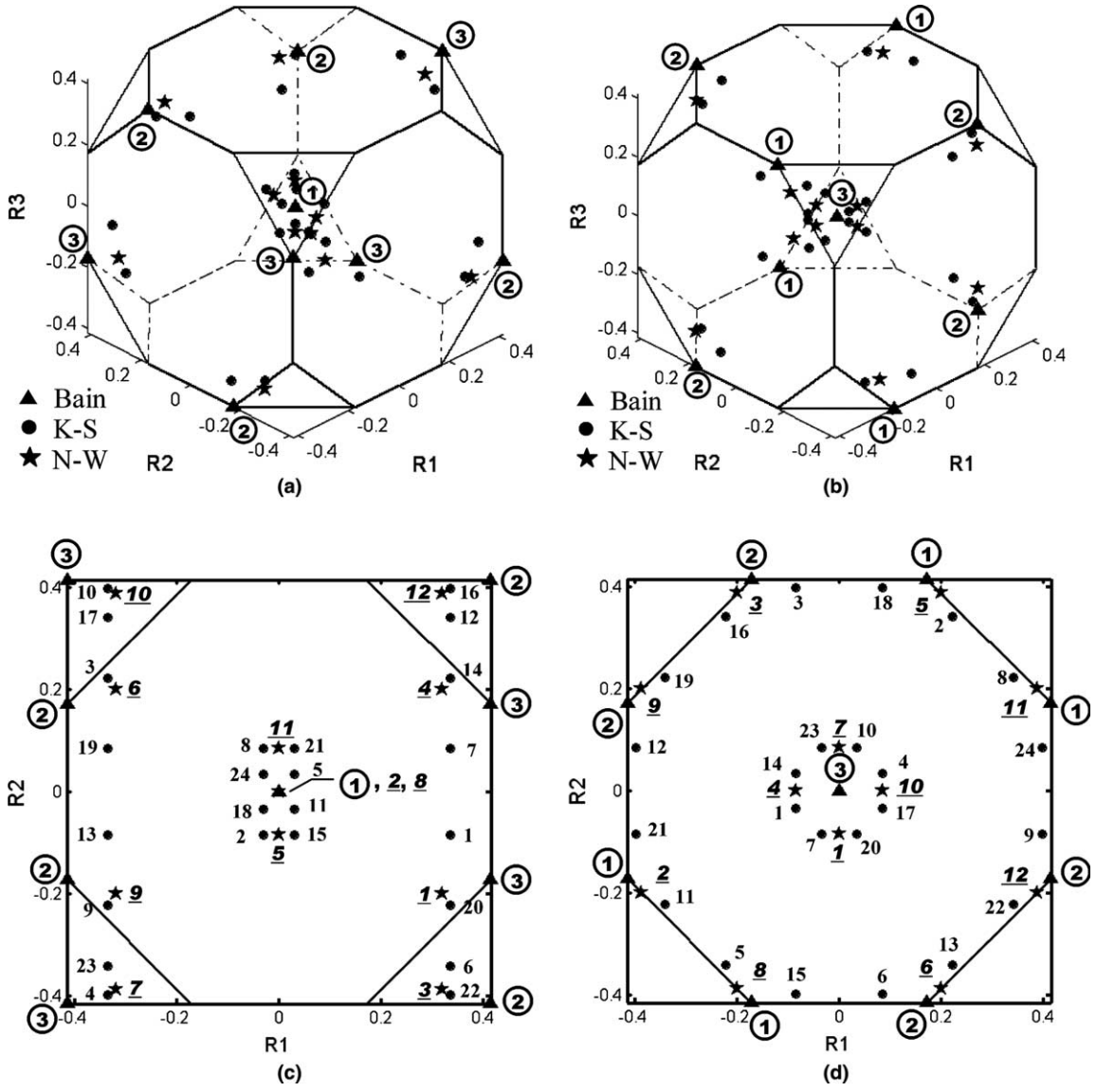

Fig. 4. The Bain, K–S and N–W relationships in R–F space with one of the Bain variants taken as the reference system: (a) Bain variant 1 as reference, (b) Bain variant 3 as reference, (c) projection of (a) onto the bottom face, (d) projection of (b) onto the bottom face. Here, only 12 N–W points can be seen. Circled and underlined numbers represent the Bain and N–W variants, respectively.

the *two* opposite faces. This corresponds to two equivalent points (in addition to the first) for a total of three (multiplicity of 3). Finally, a point that resides on a *vertex*, and is thus shared by three faces, has *three equivalents* (multiplicity of 4) on the corresponding opposite faces. This is the case for the remaining Bain variants when one Bain variant is taken as the reference, as pointed out above.

The misorientations between the Bain, K–S and N–W variants can be readily calculated once all the variants have been identified. Between the Bain variants, these are 62.8° $\langle 1\,1\,(\sqrt{2}-1)\rangle$, represented as angle–axis pairs. Thus, the misorientation between two Bain variants takes the maximum allowable value of disorientation angle between two cubic crystallites [20]. From Fig. 4(b), it is apparent that each K–S variant has two close neighbors, each with an R–F misorientation angle of 10.53°. For example, the two closest neighbors of variant 1 are 14 (coplanar variant) and 7 (cross-slip related variant), with misorientations of 10.53° $[0\,1\,-1]_\alpha$ and 10.53° $[1\,1\,1]_\alpha$, respectively. By contrast, the misorientation between two adjoining N–W variants is 13.76°; e.g. the two closest neighbors of N–W variant 1 are 4 and 10, with misorientations of 13.76° $[-0.706\ 0.06\ -0.706]_\alpha$ and 13.76° $[0.706\ -0.06\ -0.706]_\alpha$, respectively. The misorientation between one N–W variant and its two nearest K–S neighbors is 5.26° $\langle 1\,1\,0\rangle_\alpha$.

In Fig. 4, the 24 K–S and 12 N–W variants are distributed on the surfaces of four spheres (two inner and two outer) centered on the origin. The radii of the inner

spheres for K–S and N–W are 0.097 and 0.085, respectively. These distances are calculated from misorientations of 11.07° $\langle 0.879\ 0.364\ 0.307\rangle_\alpha$ and 9.74° $\langle 1\,0\,0\rangle_\alpha$, respectively. There are eight K–S variants and four N–W variants on the surfaces of these inner spheres. The radii of the outer spheres for K–S and N–W are 0.526 and 0.538, respectively. These correspond to misorientations of 55.53° $\langle 0.419\ 0.648\ 0.636\rangle_\alpha$, 55.53° $\langle 0.162\ 0.754\ 0.636\rangle_\alpha$ for the K–S variants and 56.60° $\langle 0.717\ 0.371\ 0.590\rangle_\alpha$ for the N–W variants. There are 16 K–S variants and eight N–W variants on the surfaces of these outer spheres.

4. Application to misorientations in the Gibeon meteorite

Iron meteorites have long been of interest to metallurgists because of their special microstructural and crystallographic characteristics. These materials pass through the γ-to-α phase transformation at cooling rates of 0.1–500 °C/million years [21], which cannot of course be reached under laboratory conditions. Iron meteorites usually consist of two major phases, kamacite and taenite, as well as their eutectoid mixture, plessite [21]. Kamacite is the BCC α phase known to metallurgists as ferrite, while taenite is the FCC γ phase known as austenite [22]. Plessite is an intimate mixture of kamacite and taenite consisting of tiny α and γ grains. The most interesting feature of iron meteorites is the very coarse Widmanstätten structure that forms by diffusion-controlled nucleation and growth at these extremely slow cooling rates. The Widmanstätten pattern is developed when the individual lamellae of kamacite thicken by solid-state diffusion and eventually contact one another. Some traces of the precursor phase almost always remain as rims or "blebs" between or within the kamacite lamellae. Their presence makes it possible to determine the orientation of the prior austenite phase.

Some typical microstructures of the Gibeon meteorite (belonging to group IVA, fine octahedrite, discovered in Gibeon, Namibia) are illustrated in Fig. 5. In this figure, the colors of the kamacite lamellae are associated with crystal orientation differences. The white rims between and within the kamacite grains consist of taenite. Numerous Neumann bands (mechanical twins) can also be seen across and within the individual kamacite grains. Plessite regions are separated from kamacite lamellae by taenite rims.

The Widmanstätten patterns in iron meteorites not only display special microstructural features, but also provide evidence of specific orientation relationships between the kamacite lamellae and the retained taenite rims.These relationships have been investigated by means of X-ray diffraction [23], TEM [24] and neutron diffraction [25]. The results obtained have produced evidence for both the K–S and N–W relationships, as well as for intermediate orientations. More recently, Bunge et al. [26] measured the orientation distribution of the Widmanstätten plates in a sample of the Gibeon meteorite using high-energy synchrotron radiation. Their measurements revealed a continuous range of orientations stretching out from the N–W orientation to both of the adjoining K–S orientations. However, the orientation relationship between the taenite and kamacite in the plessite regions was not studied intensively. Nevertheless, an investigation by Hasan and Axon [24] using TEM indicated that there was a near- K–S relationship between the two phases.

Some typical EBSD maps obtained from the Gibeon meteorite are illustrated in Fig. 6. The large plate-like grains in the upper part are kamacite (BCC) lamellae. At the bottom of these maps, there is a plessite region that consists of tiny kamacite plates (about 2–4 μm wide) and taenite particles (1 μm or less in diameter). In the 844 μm × 1068 μm scanned area, the taenite (FCC) phase (including the tiny grains in the plessite region) shares essentially the same orientation, as shown in Fig. 7(a). The mean orientation of the measured taenite points is ($\varphi_1 = 101.8°$, $\Phi = 51.0°$, $\varphi_2 = 28.7°$), with an average deviation of 4.4°. If the taenite orientation and its immediately neighboring kamacite orientations are compared, orientation relationships close to both N–W and K–S are observed, usually a few degrees away from the exact N–W or K–S variants.

In the plessite region, the tiny kamacite (BCC) grains are also related to the parent taenite phase by relationships that are close to K–S or N–W. This is shown in Fig. 7(b), where the variants predicted by the Bain, K–S and N–W relationships based on the mean orientation of the taenite phase are superimposed on the measured kamacite orientations. It can be seen that the observed orientations are distributed continuously along the line of the three coplanar N–W and K–S variants. A continuous spread of orientations is also observed between the two non-coplanar but cross-slip-related K–S variants, though with lower density. This corresponds to the neighborhood of the Pitsch orientation, as considered below in more detail, and resembles the orientation relationships between the kamacite lamellae and the taenite reported by Bunge et al. [26]. It should be noted, however, that the Bain relationship is not observed.

These relationships are seen more clearly in R–F space, as shown in Fig. 8. The measured kamacite orientations are compared against the predictions obtained from the K–S (Fig. 8(a)) and N–W (Fig. 8(b)) relationships. In these cases, the axes of the average taenite orientation were chosen for reference. From this figure, it is evident that the measured kamacite orientations are spread over both the K–S and N–W locations, which means that both of these relationships were obeyed. It

should be added that for the N–W relationship, all 24 R–F vectors (including the 12 equivalents induced by the symmetry rotations) should be employed to evaluate the experimental data since data points that are not *exactly* on the surface will have only one reflection and should be considered as either near one N–W variant

Fig. 5. Typical microstructures of the Gibeon meteorite: (a) kamacite lamellae (K), (b) taenite (T) and plessite (P). Etched using an aqueous solution containing 10% sodium thiosulfate and 3% potassium metabisulfite.

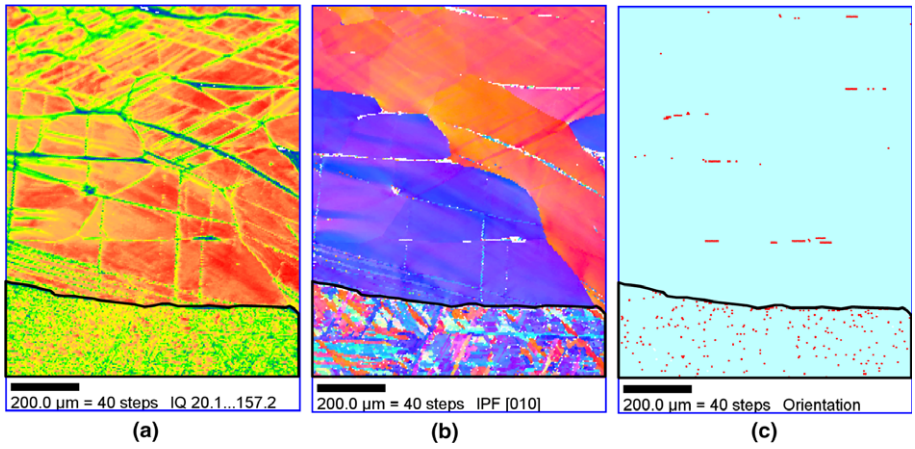

Fig. 6. EBSD maps for the Gibeon meteorite: (a) image quality map for the kamacite and taenite, (b) inverse pole figure map of the kamacite, (c) orientation map of the taenite.

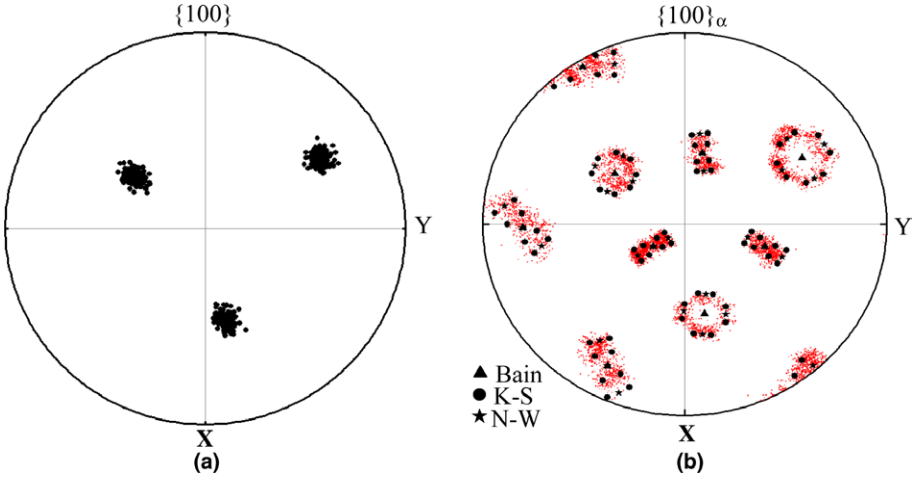

Fig. 7. {001} pole figures of the taenite and kamacite phases in the plessite region: (a) taenite (FCC), (b) kamacite (BCC), both measured and predicted.

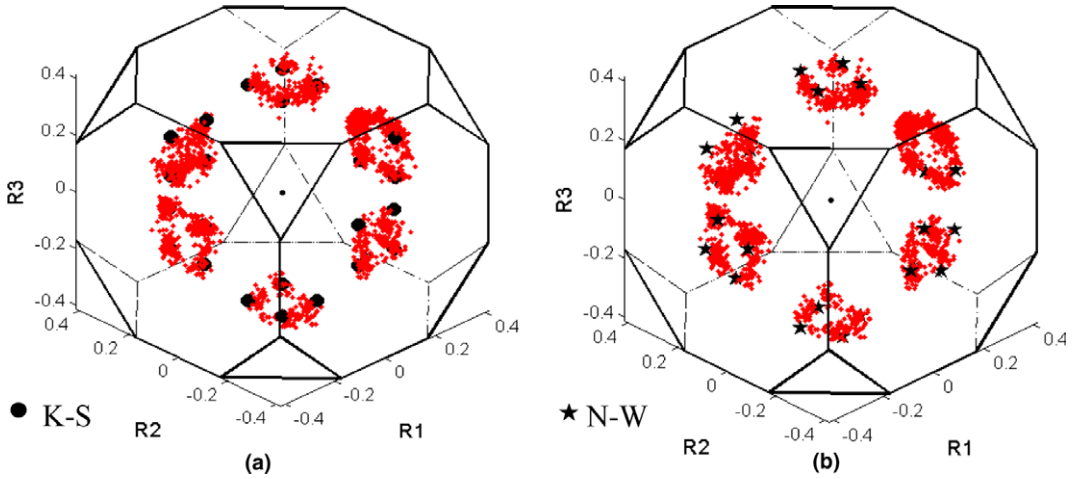

Fig. 8. Measured kamacite orientations in the plessite region as represented in R–F space: (a) compared with the predicted K–S variants, (b) compared with the predicted N–W variants. The average taenite orientation is taken as the reference.

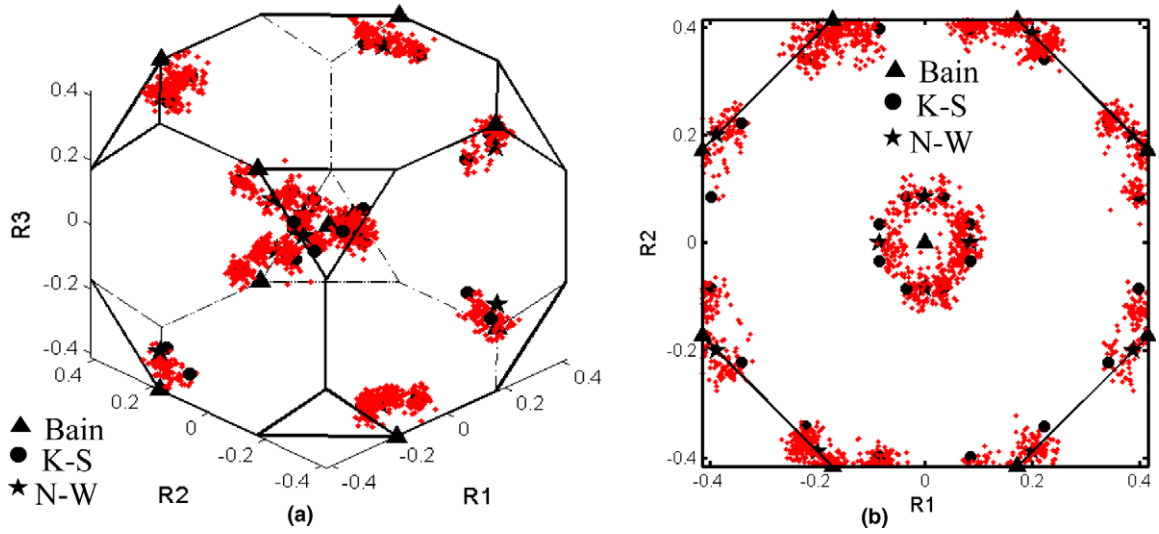

Fig. 9. Orientation relationships in R–F space referred to one of the Bain variants: (a) 3-D view of the predicted and measured variants, (b) projection onto the bottom face.

or near its equivalent on the opposite face. Moreover, all 24 variants predicted by both the K–S and N–W forms of representation appear to be present and evenly distributed in R–F space. This indicates that no variant selection occurred under the ''equilibrium'' cooling conditions that applied in the present case.

In Appendix A, some further kamacite observations are presented in R–F space, but compared with the predictions of the Pitsch correspondence relations.

Fig. 9 shows the measured taenite and kamacite orientation relationships in the plessite region as referred to one of the Bain variants. Here, the observations are again compared with the predictions. In this case, they indicate in more detail that both the K–S and N–W relationships are satisfied, with almost all the measured points in the vicinities of the variants predicted by the two sets of correspondence relations. It is of particular note that the Bain relationship is never observed.

5. Conclusions

1. Three of the correspondence relationships (the Bain, K–S and N–W) that describe the γ-to-α transformation have been represented in R–F space with the γ crystal chosen as the reference system. The Bain and N–W variants are seen to be symmetrically distributed on the boundary surfaces of the fundamental

zone. By contrast, the K–S variants are located on the faces of an *inner* cube located within the fundamental zone. The Bain, K–S and N–W relationships are associated with 6, 24 and 24 endpoints, respectively, in the fundamental zone.

2. When one of the Bain variants is chosen as the reference system, the neighboring K–S and N–W variants are located on the surfaces of two inner spheres; their radii are 0.085 and 0.097 for the N–W and K–S variants, respectively. The two remaining Bain variants are situated at selected vertices of the fundamental zone, with each variant being represented by four equivalent points on the boundary faces. In this case, the relationship between the Bain, K–S and N–W variants resembles that of the pole figure representation, particularly when an appropriate 2D projection of R–F space is employed.
3. Observations regarding the transformation of γ to α in the plessite region of the Gibeon meteorite were carried out by means of an automatic EBSD technique. Analysis reveals that both the K–S and N–W relationships are obeyed, together with all those called for by the intermediate direction parallelism conditions. By contrast, the Bain relationship is never observed.
4. Most of the measured orientations are distributed around the three coplanar K–S and N–W variants; a smaller number are located adjacent to the two cross-slip-related K–S variants. Essentially all the K–S and N–W variants are observed without any variant selection.

Appendix A. Crystallographic features of the Pitsch relationship and applicability to the present results

The Pitsch relationship was originally proposed in 1962 [27] and can be described as follows: $\{100\}_\gamma // \{110\}_\alpha$ $\langle 0-11\rangle_\gamma // \langle 1-11\rangle_\alpha$. It applies principally to precipitation in cubic systems, such as Cu–Cr, and has been observed and reported by numerous researchers [28–32]. Here, it is of interest to describe the features of this transformation relation in R–F space, to compare these to those of K–S and N–W, and then to assess the present results in terms of the degree to which the present observations satisfy the above parallelism conditions.

The conditions themselves lead to 24 possible rotation axes. However, as was the case for the N–W relationship, 12 of these are redundant, so that there are only 12 (and not 24) physically distinct variants, see Table A1. The locations of the **P** rotation axes in R–F space are compared with those of the K–S and N–W axes, respectively, in Fig. A1(a) and (b). These

Table A1
The Bain and Pitsch variants

Bain variant	Pitsch variant	$\{001\}_\gamma // \{110\}_\alpha$	$\langle 110\rangle_\gamma // \langle 111\rangle_\alpha$
1	2	(001)//(1−10)	[110]//[11−1]
	5	(010)//(−10−1)	[−101]//[−1−11]
$(100)_\gamma // (100)_\alpha$	8	(001)//(−1−10)	[−110]//[−11−1]
$[010]_\gamma // [011]_\alpha$	11	(010)//(10−1)	[101]//[1−11]
2	3	(100)//(01−1)	[011]//[−111]
	6	(001)//(−1−10)	[1−10]//[1−1−1]
$(010)_\gamma // (010)_\alpha$	9	(100)//(0−1−1)	[0−11]//[−1−11]
$[001]_\gamma // [101]_\alpha$	12	(001)//(−110)	[110]//[11−1]
3	1	(010)//(−101)	[101]//[1−11]
	4	(100)//(0−1−1)	[01−1]//[−11−1]
$(001)_\gamma // (001)_\alpha$	7	(010)//(−10−1)	[10−1]//[1−1−1]
$[100]_\gamma // [110]_\alpha$	10	(100)//(0−11)	[011]//[−111]

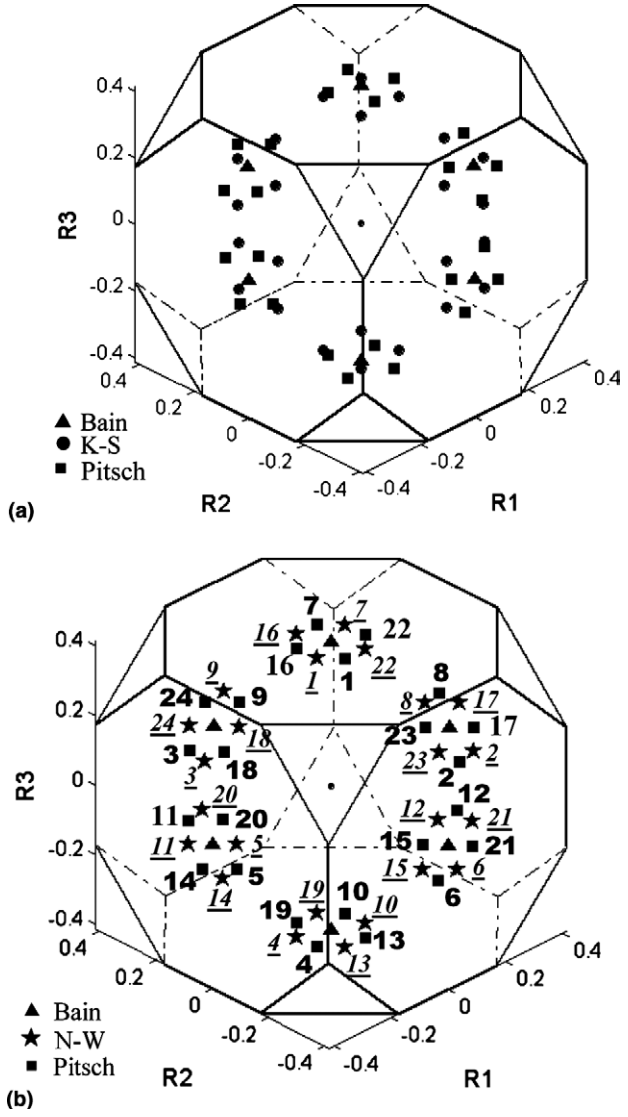

Fig. A1. (a) The Bain, K–S and Pitsch relationships in RF space. (b) The Bain, N–W and Pitsch relationships in RF space. The NW and Pitsch variants are numbered according to Tables 2 and A1, respectively.

axes are distributed around the Bain positions in much the same way as the N–W axes. (Note that the rotation angle ϖ is identical and that the components of the R–F vector are also identical, but are simply permuted in a different manner.) As a result, the sets of P and N–W axes are simply related by a rotation of 45° about the Bain axis.

This is seen to better effect in Fig. A2(a), where the positions of the K–S, N–W and P rotation axes are projected onto the bottom face of the R–F cube using the parent austenite as the reference frame. Although the N–W and P axes appear to be superimposed they are situated on opposite faces (upper and lower) of the cube. It is worthy of note that the P axes are located on the *surface* of the cube, as are the N–W axes, while the K–S axes are slightly displaced towards the center. A similar plot, but employing the Bain reference frame in this case, is presented in Fig. A2(b). Here, the P axes display a multiplicity of two around the periphery because they are situated on the faces (octahedral faces or truncated triangular corners).

The relative positions of the K–S, N–W and P reflections are illustrated on a {001} pole figure in Fig. A3. As indicated above, the N–W reflections are located between two "co-planar" K–S reflections, while the P reflections are situated midway between two K–S reflections that are "cross-slip" related (in terms of the Bishop and Hill notation).

A {001} pole figure displaying the measured orientations of the kamacite plates within a single taenite grain is displayed in Fig. A4(a). Here, it can be seen that the observations are clustered around the K–S and N–W positions, while the intensities in the neighbourhood of the P axes are relatively low. There are no reflections in the Bain position. The same measurements are illustrated on the R–F cube in Fig. A4(b), where once again the lack of correspondence with the rotation axes that correspond to the P parallelism conditions is readily evident.

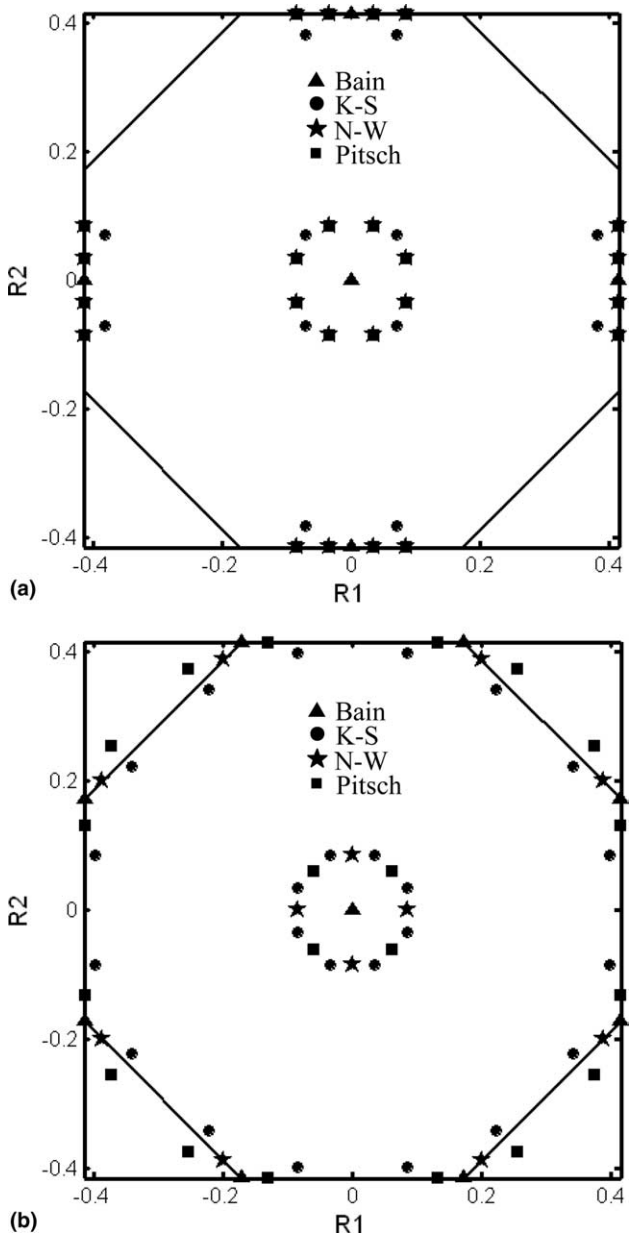

Fig. A2. (a) The Bain, K–S, N–W and Pitsch relationships in RF space. Projection onto the bottom face, with the parent austenite orientation as the reference frame. (b) The Bain, K–S, N–W and Pitsch relationships in RF space. Projection onto the bottom face, with Bain variant 3 taken as the reference frame.

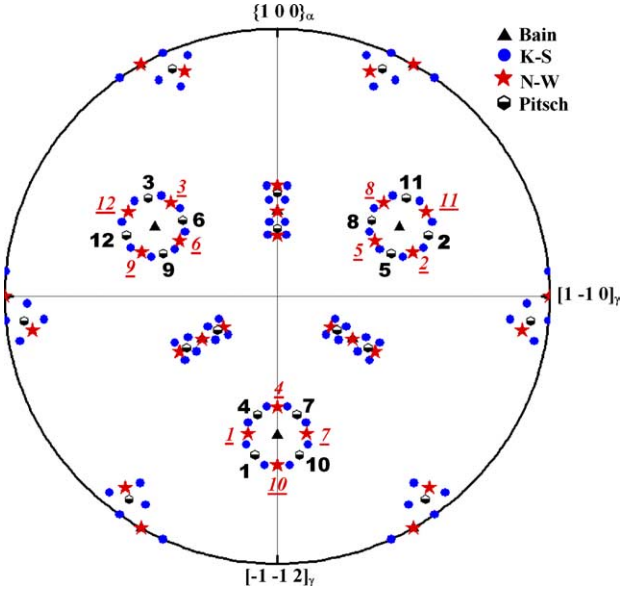

Fig. A3. Stereographic plot of $\{100\}_\alpha$ poles for the Bain, K–S, N–W and Pitsch variants projected onto the $(111)_\gamma$ plane. The N–W variants (underlined) and Pitsch variants are numbered according to Tables 2 and A1, respectively.

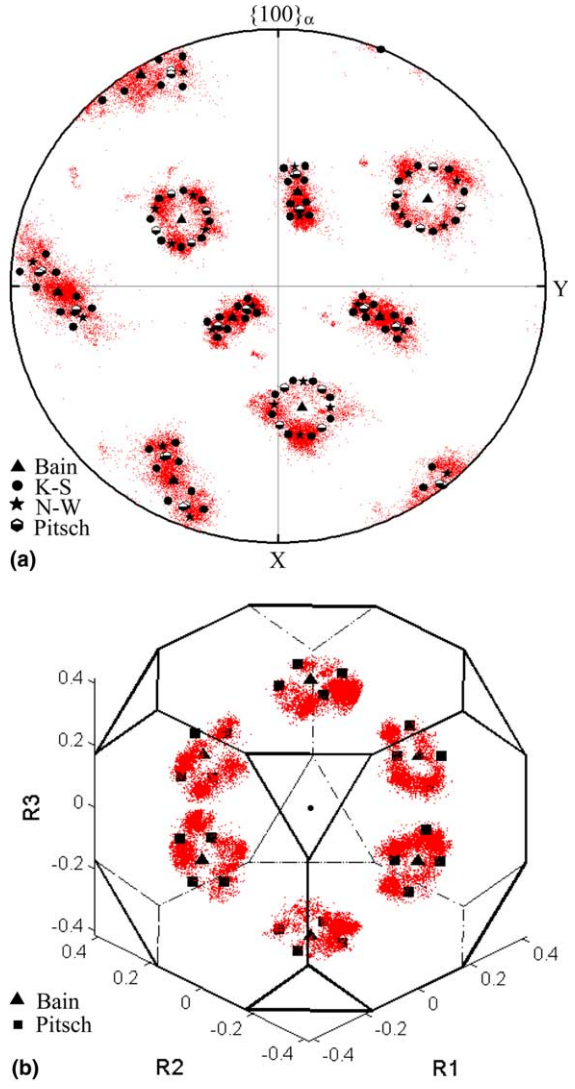

Fig. A4. (a) {001} pole figure for the kamacite. (b) The kamacite orientations in R–F space; the Bain and Pitsch orientation relationships are also displayed.

Conclusions

1. The Pitsch relations can be described in terms of the same rotation angle as the one that applies to the N–W relationship and the magnitudes of the R–F vector components are identical, except that they are permuted in a different order. This leads to considerable similarity between the distributions of the P and N–W reflections around the Bain position in a pole figure (there is a rotation angle of 45° between the two sets).
2. The present observations indicate that the Bain transformation is never observed, that both the K–S and N–W correspondence relations apply to the bcc phase in the Gibeon meteorite, but that few reflections are located in the vicinities of the Pitsch rotation axes.

References

[1] Randle V. The measurement of grain boundary geometry. London: Institute of Physics Publishing; 1993.
[2] Godet S, Glez JC, He Y, Jonas JJ, Jacques PJ. J Appl Crystallogr 2004;37:417.
[3] Frank FC. Metall Trans A 1988;19:403.
[4] Becker R, Panchanadeeswaran S. Texture Microstruct 1989;10:167.
[5] Randle V, Day A. Mater Sci Technol 1993;9:1069.
[6] Randle V. Proc R Soc Lond A 1990;431(1881):61.
[7] Randle V, Engler O. Introduction to texture analysis: macrotexture, microtexture and orientation mapping. Amsterdam: Gordon and Breach Publishing Group; 2000.
[8] Bain EC. Trans AIME 1924;70:25.
[9] Kurdjumov G, Sachs G. Z Phys 1930;64:225.
[10] Nishiyama Z. Sci Rep Res Inst Tohoku Univ 1934–35;23:638.
[11] Wassermann G. Arch Eisenhüttenwes 1933;16:647.
[12] Pitsch W. Acta Metall 1962;10:897.
[13] Kuipers JB. Quaternions, rotation sequences: a primer with applications to orbits, aerospace, and virtual reality. Princeton: Princeton University Press; 1999.
[14] Rodrigues OJ. de Mathématiques Pures et Appliquées 1840; 5:380.
[15] Kumar A, Dawson PR. Comput Methods Appl Mech Eng 1998;153:259.
[16] Ray RK, Jonas JJ. Int Mater Rev 1990;35(1):1.
[17] Bishop JF, Hill R. Philos Mag 1951;42:414.
[18] Bishop JF, Hill R. Philos Mag 1951;42:1298.
[19] Wittridge NJ, Jonas JJ, Root JH. Metall Mater Trans A 2001;32(4):889.
[20] Mackenzie JK. Biometrika 1958;45(1/2):229.
[21] Buchwald VF, editor. Handbook of iron meteorites: their history, distribution, composition and structure, vols. I–III. Berkeley: University of California Press; 1975.
[22] Voort GFV. Mater Charact 1992;29:223.
[23] Young J. Proc R Soc Lond A 1926;112:630.
[24] Hasan F, Axon AJ. J Mater Sci 1985;20:590.
[25] Höfler S, Will G, Hamm HM. Earth Planet Sci Lett 1988;90:1.
[26] Bunge HJ, Weiss W, Klein H, Wcislak L, Garbe U, Schneider JR. J Appl Crystallogr 2003;36:137.
[27] Pitsch W. Acta Metall 1962;10:897.
[28] Hall MG, Aaronson HI, Kinsman KR. Surf Sci 1972;31: 257.
[29] Dahmen U, Ferguson P, Westmacott KH. Acta Metall 1984;32:803.
[30] Luo CP, Weatherly GC. Acta Metall 1987;35:1963.
[31] Fujii T, Mori T, Kato M. Acta Metall Mater 1992;12:3413.
[32] Naik R, Kota C, Payson JS, Dunifer GL. Phys Rev B 1993;48:1008.